-RESEARCH PAPER-

International Journal of Mining and Geo-Engineering

IJMGE

IJMGE 58-2 (2024) 153-160

DOI: 10.22059/IJMGE.2024.367235.595113

Time-Domain Induced Polarization Tomography Inversion

Seyyed Sajjad Pourhashemi [a], Reza Ghanati [a, *], Ashkan Aliheidari [a]

[a] *Institute of Geophysics, University of Tehran, Iran.*

Article History:

Received: 25 October 2023.

Revised: 02 January 2024.

Accepted: 09 January 2024.

ABSTRACT

Induced polarization (IP) tomography measurements, as a near-surface geophysical method, can provide information about the degree of chargeability of subsurface materials and are commonly used in mineral exploration, engineering studies (e.g., sediment/bedrock interface identification, crushed zones and faults detection, and landslide and soil properties imaging), as well as in environmental investigations (contaminant plums identification and landfill characterization). The purpose of these measurements is to obtain the distribution of polarizability characteristics inside an object, generally below the surface, at the boundary of the object, or outside the area in question. The results of such measurements can be mathematically modeled for the specific polarizability properties by solving the Poisson's equation restricted by appropriate boundary conditions. In this paper, we focused on the importance of simulating induced-polarization responses and retrieving chargeability distributions in geo-materials to enhance the characterization of subsurface structures. We presented the methods for forward modelling and non-linear inversion of IP measurements. To this end, in the first step, the Poisson's equation for a two-dimensional ground with an arbitrary distribution of conductivity is solved using the finite difference numerical method. In the next step, based on the existing relations between conductivity and chargeability (the Siegel's formulation), the apparent IP response is calculated. Finally, we solved the non-linear chargeability inversion problem following a non-linear apparent resistivity inversion. This is achieved by imposing physical constraints to prevent the estimation of unrealistic model parameters, using a Newton-based optimization method. To evaluate the efficiency of the proposed methodology, we utilized the proposed algorithm on two simulated examples and a real data set. Our numerical results show that the algorithm reliably represents the main features and structure of the Earth's subsurface in terms of resistivity and chargeability models. All the algorithms presented in this paper have written in the MATLAB programming language.

Keywords: *Finite difference, Newton-based method, Non-linear inversion, Poisson's equation, Time domain induced polarization, Tomography.*

1. Introduction

Historically, IP tomography measurements, as a non-invasive and near-surface geophysical method, have been widely used for exploring metallic ore deposits. However, in recent years, it has been increasingly utilized in a wide range of engineering and environmental applications. IP measurements are performed in two different time and frequency domains. Depending on the type of signal injected into the ground, there is a difference in the type of response recorded. Naturally, in the frequency domain, we would face more information from measurements and due to the existence of more interpretive parameters, the uncertainty in modelling and interpretation of subsurface structures decreases. Frequency domain surveys, conducted at specific frequencies, can be time-consuming and costly, and equipment availability may be limited. Hence, due to the project's time sensitivity, time domain surveys are typically preferred. A review of the induced-polarization method can be found in [1-3]. Besides advances in the foundational comprehension of induced polarization phenomena, the TDIP tomography method has shown growing progress and significant developments in many fields of research from forward modelling to inversion in recent years. Early inversion algorithms parameterized the ground model into blocks with low numbers and maintained the same for inversions [4-6]. The systems of overdetermined equations were solved and the convergence of the algorithm was judged solely on the basis of misfit. But due to the complexity of the structure of the electrical conductivity of the Earth, the display of several blocks does not adequately show the actual distribution of this physical property. This problem can be solved to alarge extent of model parameters by discretizing the terrain to a large number of blocks, and solving the inversion problem as an optimization process, where a model objective function is minimized to achieve a relatively sufficient fit to the data. The very first effort to model the effect of the presence of chargeable material on the effective resistivity was based on the study by [7]. Following the model presented by [7], [8] proposed a two-step inversion approach to retrieve a chargeability model. Their method was based on the DC resistivity inversion in the first step, and in the second step, assuming that the DC resistivity inversion estimates the effective resistivity model instead of the intrinsic resistivity model, the chargeability model is inverted. [9] suggested a 2D inversion of the IP data in specular cross-section tomography experiments. [10] presented an approximate inversion of the IP data which is valid for low resistivity contrasts. Later, [11] extended this approach to the 3D inversion of the IP data. [12] developed a computationally simpler method based on a low-contrast (resistivity and chargeability) approximation. However, this approach has now diminished in value due to subsequent computational advancements. [13] developed a software for time-lapse two- and three-dimensional IP data. Despite progress in the application of the TDIP method, the principles behind the inversion of resistivity and IP data have not really

* Corresponding author. *E-mail address:* rghanati@ut.ac.ir (R. Ghanati).

changed in recent years.

In this paper, [7] and the algorithm proposed by [8], we present a two-step inversion of the IP data in which the resistivity data are first inverted, and at the second step, the polarizability model is recovered using a non-linear chargeability inversion. In the non-linear inversion, the non-linearity of the underlying problem is linearized using a sensitivity matrix containing partial derivatives of measurements with respect to model parameters. The most obvious way to determine these entries is the application of the forward matrix method which is rather time-consuming [13].

In the following, we first provide the theory and mathematical formulation of the DC resistivity and IP forward modelling. Next, we present a non-linear inversion method under spatial smoothness constraints aimed at retrieving resistivity and chargeability models. We then evaluate the efficiency of our approach using both synthetic and field data sets of the IP. We end the paper with conclusions.

2. Methodology

IP measurements are usually accompanied with direct current resistivity measurements. The merit of utilizing IP method alongside pure direct current lies in the difficulty of detecting the resistivity signature caused by disseminated chargeable material. The chargeability signature resolved by the IP method may be strong and relatively independent of the geometry of the resistivity structure. When subjecting the ground to an external field, in the specific form of direct current (low-frequency current), the potential experiences a rapid and sudden increase in the absence of chargeability referred to as the instantaneous potential (V_∞). This increase is followed by a gradual and exponential growth until it reaches a steady and constant value. This final value, which is utilized to determine the apparent resistivity, is commonly referred to as the primary potential (V_p). When the electrical field is interrupted, there is an initial sharp drop in potential, known as the secondary potential (V_s), which then decreases exponentially as the charges return to their initial state. This subsequent potential change is influenced by the polarizability characteristic of the Earth. However, in real data, it is not feasible to measure the secondary potential, because it corresponds to the moment of current transmission. Therefore, it cannot be practically measured and is solely defined theoretically in the context of forward modelling relations [8].

[7] first defined the principal concept of chargeability as a physical property and demonstrated that the IP response (η_a is influenced by the subsurface distribution of intrinsic chargeability. Building upon the work of [7], the IP response of a uniform earth with the intrinsic conductivity (σ_∞) and intrinsic chargeability (η) is expressed as:

$$\eta_a = \frac{f_{dc}(\sigma_\infty(1-\eta)) - f_{dc}(\sigma_\infty)}{f_{dc}(\sigma_\infty(1-\eta))} \quad (1)$$

where f_{dc} stands for the direct current resistivity forward operator. It is noteworthy that the terms $f_{dc}(\sigma_\infty(1-\eta))$ and $f_{dc}(\sigma_\infty)$ are proportional to the V_p and V_s, respectively. Equation 1 reveals that the apparent chargeability is computed based on two consecutive applications of the resistivity forward operator for two conductivity models, that is, $\sigma_\infty(1-\eta)$ and σ_∞. The forward modelling of electrical potential due to an arbitrary conductivity distribution and for a point source is expressed in terms of the Poisson's equation [14].

$$-\nabla.(\sigma_\infty \nabla V_\infty) = I\,\delta(r - r_s) \quad (2)$$

where V_∞ is the potential measured in the absence of chargeability, I indicates the injected current, r_s is the position of the point sources of the current electrode, and δ is the Dirac delta function.

Assuming $\vec{E}$ is the external field, the applied current density vector is $\vec{j} = \sigma_\infty \vec{E}$. The vector $\vec{j}(1-\eta)$ plays the role of $\vec{j}$ when there is a distribution of dipoles. Therefore, the total current density at the time of the existence of dipoles in the ground with chargeability is equal to $\sigma_\infty(1-\eta)\vec{E}$, and the net effect is to reduce σ_∞ by factor $(1-\eta)$. Using Siegel relations, the ground chargeability effects are simulated by employing the forward operator of the DC resistivity f_{dc} with effective conductivity $\sigma_\eta = \sigma_\infty(1-\eta)$, [7]:

$$V_\eta = f_{dc}[\sigma_\infty(1-\eta)]. \quad (3)$$

Insertion Equation 3 into Equation 2 yields:

$$-\nabla.\left(\sigma_\infty\,(1-\eta)\nabla V_\eta\right) = -\,I\,\delta(r - r_s) \quad (4)$$

It is noticed that in contrast to Equation 2 in which the chargeability is neglected, Equation 4 includes polarization effects. From a practical point of view, the potential V_η is usually measured that should be inverted to retrieve the intrinsic conductivity σ_∞, but the inversion of V_η results in the conductivity σ_η. The crucial initial step, as indicated by Equations 2 and 4, is to formulate and solve a 2.5D electrical resistivity forward modelling problem. The merit of the 2.5D method lies in its ability to achieve a physically realistic representation, incorporating the full 3D electrical potential distribution. This is accomplished by addressing multiple problems within a constrained 2D geometry, considering various wavenumbers. Consequently, computational time is minimized compared to performing a complete 3D forward modelling. The computation of electrical resistivity forward responses involves simulating current flow into the Earth's surface by solving the Poisson's equation. This is achieved through the finite difference approximation, utilizing mixed boundary conditions as proposed by [15]. The 3D distribution of electrical potential due to a point source $r_s = (x_s, y_s, z_s)$ is expressed by the following governing equation [15]:

$$\nabla \cdot [\sigma_\infty(\mathrm{x,y,z})\nabla V_\infty(x,y,z)] = -I\delta(x-x_s)\delta(y-y_s)\delta(z-z_s). \quad (5)$$

To account for the three-dimensional source characteristic, we need to the Fourier transform the partial differential equation (5) with respect to y, the strike direction, using the cosine transform [15]:

$$\tilde{V}_\infty(x,k_y,z) = \int_0^\infty V_\infty(x,y,z)\cos(k_y y)\,dy, \quad (6)$$

where $\tilde{V}_\infty$ stands for the transformed potential in the wavenumber domain and k_y is the wavenumber with respect to y.

Applying the Fourier-cosine transformation to the three-dimensional Poisson's equation (5), one obtains [15]:

$$\frac{\partial}{\partial x}(\sigma_\infty(x,z)\frac{\partial \tilde{V}_\infty}{\partial x}) - k_y^2\sigma_\infty(x,z)\tilde{V}_\infty + \frac{\partial}{\partial z}(\sigma_\infty(x,z)\frac{\partial \tilde{V}_\infty}{\partial z}) = -\frac{I}{2}\delta(x-x_s)\delta(z-z_s) \quad (7)$$

Equation (7) is numerically solved using rectangular or triangular mesh discretization procedure. After obtaining discrete representations for the principle governing equations and boundary conditions at all cells, the transformed forward problem can be represented as a linear system of equations:

$$\mathbf{C}\tilde{V}_\infty = \boldsymbol{q}, \quad (8)$$

where $\mathbf{C}$ indicates a real sparse five-band symmetric matrix and $\boldsymbol{q}$ displays the source vector. This equation has to be solved for the vector $\tilde{V}_\infty$ containing the potentials for all existing nodes. By taking the advantage of the sparsity of the matrix $\mathbf{C}$, it is possible to use direct methods that can be computationally efficient. The solution $\tilde{V}_\infty$ is then transformed from the wavenumber domain to the spatial domain (i.e., x-z plane) following the procedure of [15] and based on the inverse cosine-Fourier transform [15],

$$V_\infty(x,z) = \frac{2}{\pi}\int_0^\infty \tilde{V}_\infty(x,k_y,z)\cos(k_y y)\,dK_y. \quad (9)$$

The next step is to formulate the inverse problem of electrical resistivity tomography data.

3. Inversion of electrical resistivity tomography data

The inverse problem of electrical resistivity tomography (ERT) data is formulated as a non-linear problem and is usually solved through an iterative process that applies a forward modelling for arbitrary resistivity distribution. The relationship between the observed data and model parameters is defined as:

$$\mathbf{d} = \boldsymbol{f}(\mathbf{m}). \quad (10)$$

By linearizing Equation 10 using a first-order Taylor expansion, we have:

$$\Delta\mathbf{d} = \nabla\boldsymbol{f}(\mathbf{m})\Delta\mathbf{m}. \quad (11)$$

In these equations, $\mathbf{d} \in \mathcal{R}^{m\times 1}$ is the observed data, $\mathbf{m} \in \mathcal{R}^{n\times 1}$ is the model parameters (here, $\mathbf{m}$ includes the subsurface conductivity distribution), $\boldsymbol{f}(\mathbf{m}) \in \mathcal{R}^{m\times n}$ is the non-linear forward operator, $\Delta\mathbf{d} = \mathbf{d} - \boldsymbol{f}(\mathbf{m})$ is a vector of the difference between observed and theoretical data, $\nabla\boldsymbol{f}(\mathbf{m})$ is a sensitivity matrix that represents the changes in the response of the forward modelling to changes in the model parameters with elements $J_{i,j} = \frac{\partial \mathrm{d}_i}{\partial \mathrm{m}_j}$, and $\Delta\mathbf{m}$ is a model correction (perturbation) vector. In the inversion process, we seek to minimize the difference between observed and theoretical data using the following cost function: a measure of the goodness of fit between the data and the model parameters, accounting for noise [16]:

$$\Phi_{\mathbf{d}} = min||\mathbf{W}_{\mathrm{d}}(\mathbf{d} - \boldsymbol{f}(\mathbf{m}))||_{l_2}^2. \quad (12)$$

The process of solving most of geophysical inverse problems is often highly unstable, so that the smallest changes in measurements can lead to large variations in the estimated model. The ERT non-linear inversion problem is also inherently ill-posed, resulting in non-unique estimates of the model parameters. To numerically solve the inverse problem, we must consider data fidelity, model residual, and physical constraints to reduce instability of the inversion and the size/dimension of the model space to increase the chance of obtaining a geologically meaningful model. To that end, we form a weighted sum of the data fidelity $\Phi_{\boldsymbol{d}}$ and the stabilizer function $\Phi_{\mathbf{m}}$ using a weighting factor α, and find the solution which minimizes the objective function as given by:

$$\Psi(\mathbf{m},\alpha) = \min(\Phi_{\boldsymbol{d}} + \alpha\Phi_{\boldsymbol{m}}) = \min\|\mathbf{W}_d(\mathbf{d} - \boldsymbol{f}(\mathbf{m}))\|_{l_2}^2 + \alpha\left\|\mathbf{W}_{\mathrm{m}}(\mathbf{m} - \mathbf{m}_{apr})\right\|_{l_2}^2, \quad (13)$$

where α is the damping factor, $\mathbf{W}_{\mathrm{d}}$ represents the data weighting matrix, comprised of the inverse of the data error, assuming that the noise for each experiment is independently and normally distributed, $\mathbf{W}_{\mathrm{m}} = a_h\mathbf{D}_h^{\mathrm{T}}\mathbf{D}_h + \mathrm{b}_h\mathbf{D}_V^{\mathrm{T}}\mathbf{D}_V$ is the model constraint matrix, and the positive coefficients $a_h = 1$ and $b_h = 0.5$ are used to promote heightened smoothness in either horizontal or vertical directions, and $\mathbf{m}_{\mathrm{apr}}$ is the prior model. It is worth mentioning that different norms (l_p) can be used for misfit and regularization terms. When using the l_2 norm for misfit, all the data is given equal weight, leading the algorithm to be influenced by noise that falls outside the desired range. This can result in a suboptimal fit. On the other hand, when the l_1 norm is employed, the algorithm becomes less susceptible to noise; however, from a mathematical and derivational standpoint, it presents a more complex solution. Hence, utilizing the l_2 norm is preferred, because it simplifies the mathematical calculations in the context of misfit. The choice of which norm to use in the regularization term depends on the geological conditions and the specific model requirements. In models where we are seeking sharp or sparse representations, the l_1 norm is employed. Conversely, in models using the l_2 norm, we aim to obtain smoother and more continuous estimations [16].

By linearization using the Taylor expansion and replacing the first and second terms of the expansion, one obtains:

$$\min\left|\left|\mathbf{d} - \boldsymbol{f}(\mathbf{m}) - \nabla\boldsymbol{f}(\mathbf{m})\Delta\mathbf{m}\right|\right|_{l_2}^2 + \alpha\left|\left|\mathbf{W}_{\mathrm{m}}(\mathbf{m} - \mathbf{m}_{\mathrm{apr}} + \Delta\mathbf{m})\right|\right|_{l_2}^2. \quad (14)$$

By taking the derivative of the objective function with respect to $\Delta\mathbf{m}$ and solving the objective function produces the following iterative numerical method, i.e.

$$\Delta\mathbf{m} = (\boldsymbol{J}(\mathbf{m}^k)^T\mathbf{W}_{\mathrm{d}}^T\mathbf{W}_{\mathrm{d}}\boldsymbol{J}(\mathbf{m}^k) + \alpha(a_h\mathbf{D}_h^{\mathrm{T}}\mathbf{D}_h + \mathrm{b}_h\mathbf{D}_V^{\mathrm{T}}\mathbf{D}_V))^{-1}\left(\boldsymbol{J}(\mathbf{m}^k)^T\mathbf{W}_{\mathrm{d}}^T\mathbf{W}_{\mathrm{d}}\Delta\mathbf{d} - \alpha(a_h\mathbf{D}_h^{\mathrm{T}}\mathbf{D}_h + \mathrm{b}_h\mathbf{D}_V^{\mathrm{T}}\mathbf{D}_V)(\mathbf{m}^{k-1} - \mathbf{m}_{apr})\right), \quad (15)$$

where $\boldsymbol{J}^T$ is the transpose of the Jacobian matrix $\boldsymbol{J}$, k shows the k-th iteration of the inversion process, and $\Delta\mathbf{m}^{k+1}$ is a search direction at the k-th iteration. The Jacobian matrix or sensitivity function is computed through a highly efficient numerical method, employing a forward matrix calculation within the context of 2.5D finite-difference electrical resistivity forward modelling. $\Delta\mathbf{d} = [\log\mathbf{d} - \log\boldsymbol{f}(\mathbf{m})]$ to ensure the positivity of the updated conductivity values. At each iteration, the algorithm is calculated by solving the objective function for $\Delta\mathbf{m}$ and the model is updated using $\mathbf{m}^{k+1} = \mathbf{m}^k + \mu\Delta\mathbf{m}$. Furthermore, before the model is updated, using a line-search algorithm, the step length μ is determined aimed at averting the iteration divergence. The minimization process is executed with a range of α values, with the objective of selecting the optimal α that results in the smoothest model while maintaining the misfit $\Phi_{\boldsymbol{d}}$ at the desired level. The motivation behind pursuing a smoother model lies in the intention to avoid being misled by non-essential features that may appear in the model but are not crucial for accurately aligning with noisy measurements. In essence, among a myriad of potential solutions (i.e., those adequately fitting the observations within a specified tolerance), our goal is to identify the simplest model—requiring the fewest unnecessary features not demanded by the observed data. This approach is commonly known as the Occam's inversion, which involves a two-step inversion process. In the initial step, the emphasis is on minimizing the misfit function within a specified tolerance (i.e., $\chi^2 = \|\mathbf{W}_{\mathrm{d}}(\mathbf{d} - \boldsymbol{f}(\mathbf{m}))\|_{l_2}^2/m$, m is the size of the data vector, moves close to one) across a range of regularization parameters. Subsequently, in the second step, the minimization of the objective function persists while maintaining the misfit function at the desired level. Moreover, the iterative process is governed by three stopping criteria; 1) the reduced-χ^2 score ($(\Phi_{\boldsymbol{d}}/m) < 1$), 2) the root mean square error (RMS = $(100 \times \sqrt{m}^{-1}\|\mathbf{d} - \boldsymbol{f}(\mathbf{m}^{k-1})\|_{l_2} < \varepsilon$, $\varepsilon = 4\%$) where m is the length of data, and 3) the number of maximum iteration is exceeded. In other words, if one of these criteria is met, the iterative process is terminated [16].

4. The inversion of time-domain IP data

[8] developed three time-domain IP inversion methods. All methods are based on the chargeability perturbation model according to [7], and they recover a resistivity and a chargeability model after two implementations of inversion. The first implementation aims to recover a resistivity model, while the second implementation is used to retrieve a chargeability model. The first method, as proposed by [8], involves solving a linear inverse problem under the assumption that the amount of chargeability is small. The second algorithm estimates the chargeability model after two resistivity inversions of perturbed resistivity models. Finally, the third method, which solves a non-linear problem, includes the most accurate theoretical framework for the inversion of the IP data. One of the advantages of this method is that it does not require that the chargeability to be small, and it uses a similar algorithm for the inversion of resistivity data and IP. Hence, we follow the third IP inversion strategy proposed by [8]. The objective function in the inversion algorithm is expressed as follows:

$$\Delta\boldsymbol{\eta} = \left(\boldsymbol{J}_{IP}(\boldsymbol{\eta}^k)^T\mathbf{W}_{\mathrm{d}}^T\mathbf{W}_{\mathrm{d}}\boldsymbol{J}_{IP}(\boldsymbol{\eta}^k) + \alpha(a_h\mathbf{D}_h^{\mathrm{T}}\mathbf{D}_h + \mathrm{b}_h\mathbf{D}_V^{\mathrm{T}}\mathbf{D}_V) + \lambda\mathbf{W}_p\right)^{-1}\left(\boldsymbol{J}_{IP}(\boldsymbol{\eta}^k)^T\mathbf{W}_{\mathrm{d}}^T\mathbf{W}_{\mathrm{d}}\Delta\mathbf{d} - \alpha(a_h\mathbf{D}_h^{\mathrm{T}}\mathbf{D}_h + \mathrm{b}_h\mathbf{D}_V^{\mathrm{T}}\mathbf{D}_V)\boldsymbol{\eta}^{k-1} - \lambda\mathbf{W}_p\boldsymbol{\eta}^{k-1}\right), \quad (16)$$

where $\boldsymbol{J}_{IP}$ is the IP sensitivity matrix as a function of the conductivity obtained from the direct current resistivity inversion, λ is a large positive value (e.g., $\lambda = 10^5$) which penalizes negative chargeability values, $\mathbf{W}_p = \underset{i}{\mathrm{diag}}(u(-\boldsymbol{\eta}))$ ($u(x)$ is the step function) displays a diagonal matrix with values of zero or one, and $\Delta\mathbf{d} = (\boldsymbol{\eta}_a - \boldsymbol{\eta}_{cal})$ is the residual vector.

The inversion begins with a uniform chargeability model ($\boldsymbol{\eta}^0$) derived from the geometric mean of the apparent chareability data as the staring model. The IP sensitiviy matrix ($\boldsymbol{J}_{IP}$) is updated at each iteration. The Jacobian matrix represents the variation of the observational data to the parameters of the model:

$$J_{IP}^{ij} = \frac{\partial \mathrm{d}_i}{\partial \eta_j}. \quad (17)$$

and

$$d_i = \boldsymbol{\eta}_a = \frac{V_\eta^i - V_\infty^i}{V_\eta^i}. \quad (18)$$

By taking the derivative of apparent chargeability with respect to η_j, we have:

$$\frac{\partial \mathrm{d}_i}{\partial \eta_j} = \frac{V_\infty^i}{(V_\eta^i)^2} \frac{\partial V_\eta^i}{\partial \eta_j}. \quad (19)$$

Algorithm 1. Pseudocode corresponding to time-domain IP data inversion

Inputs: Observed data $\boldsymbol{\eta}_a \epsilon \mathbb{R}^{m\times 1}$ including apparent chargeability measurements, the conductivity distribution σ_∞ derived from the direct current resistivity inversion, and data weighting matrix $\mathbf{W}_\mathrm{d} \epsilon \mathbb{R}^{m\times m}$.
Outputs: Inverted model parameters $\boldsymbol{\eta} \epsilon \mathbb{R}^{n\times 1}$
Initialization: define a range of α_q $(q = 1, \dots, N)$, $\mathbf{W}_\mathrm{m}$ (model constraint matrix defined as the first order roughening matrix), $\epsilon = 5\%$, $k = 1$, the initial chargeability model $\boldsymbol{\eta}^0$.
While $\chi^2 > 1$ or $(100 \times \sqrt{m}^{-1} \|\boldsymbol{\eta}_a - \boldsymbol{\eta}_a^{cal}\|_{l_2}) < \varepsilon$ or maximum iteration is not reached **do**
Comput $\boldsymbol{\sigma}_{\boldsymbol{\eta}}^{\boldsymbol{k}} = \boldsymbol{\sigma}_\infty(1 - \boldsymbol{\eta}^{k-1})$
Compute $\boldsymbol{\eta}_a^{cal} = \frac{f(\boldsymbol{\sigma}_\eta^k) - f(\sigma_\infty)}{f(\boldsymbol{\sigma}_\eta^k)}$
Compute $\Delta\mathbf{d} = (\boldsymbol{\eta}_a - \boldsymbol{\eta}_a^{cal})$ the discrepancy between the measured apparent chargeability data and the calculated one
Compute the matrix $\boldsymbol{J}_{IP}(\boldsymbol{\eta}^{k-1}) \epsilon \mathbb{R}^{m\times n}$ with respect to all model cells and meaurements
For α_q, $q = 1, \dots, N$ **do**
Compute the model perturbation $\Delta\mathbf{m}$ using Equation 16
Compute $\boldsymbol{\eta}^q = \boldsymbol{\eta}^{q-1} + \Delta\mathbf{m}$
Calculate $\boldsymbol{\sigma}_\eta^q = \boldsymbol{\sigma}_\infty(1 - \boldsymbol{\eta}^q)$
Compute $\boldsymbol{\eta}_a^{cal} = \frac{f(\boldsymbol{\sigma}_\eta^q) - f(\sigma_\infty)}{f(\boldsymbol{\sigma}_\eta^q)}$
Compue the data fidelity term $\Phi_{\boldsymbol{d}} = \|\boldsymbol{\eta}_a - \boldsymbol{\eta}_a^{cal}\|_{l_2}^2$
End for
Choose the largest value for α_q such $\chi^2 \leq 1$, otherwise select a α_q minimizing $\Phi_{\boldsymbol{d}}$
$k = k + 1$
Set $\boldsymbol{\eta}^{k-1} = \boldsymbol{\eta}^q$
End while

Now we only need to calculate $\frac{\partial V_\eta^i}{\partial \eta_j}$. By inserting $\sigma_\eta = \sigma_\infty(1 - \eta)$ as the conductivity that generates the potential V_η into Equation 19, we get:

$$\frac{\partial V_\eta^i}{\partial \eta_j} = -\sigma_\infty^j \frac{\partial V_\eta^i}{\partial \sigma_\eta^j} \equiv -\sigma_\infty^j J_{ij}, \quad (20)$$

is a scaled value of the sensitivity for a resistivity problem. σ_∞ and $J_{ij}(\sigma_\infty)$ are the intrinsic conductivity or background conductivity and the sensitivity matrix derived from the inversion of direct current resistivity inversion from the first step, respectively. The final Jacobian reads:

$$J_{IP}^{ij} = \frac{\partial \mathrm{d}_i}{\partial \eta_j} = -\sigma_\infty^j \frac{V_\sigma^i}{(V_\eta^i)^2} J_{ij}. \quad (21)$$

Algorithm 1 represents a pseudocode corresponding to the proposed inversion of IP measurements.

5. Numerical experiments

In this section, we present a set of experiments using two simulated examples and a real case from the Nikuiyeh area in Qazvin province, Northeast Iran, to demonstrate the performance and reliability of the inversion algorithm. It should be noted that in direct current resistivity surveying, the presence of negative data is generally indicative of measurement technical problems, unless the electrode arrangement's geometry yields a negative geometrical factor. Within the near surface geophysics community, it is widely believed that the same principle applies to time-domain IP measurements, where negative IP data are often considered an indication of data quality problems. Consequently, it is not uncommon to eliminate negative IP data during the data processing stage, although this practice can result in the loss of valuable information [17]. Therefore, to maintain depth resolution and prevent the formation of artifacts in the chargeability model, it is essential to retain data points with negative apparent chargeability values in both synthetic and real data sets.

5.1. Synthetic models

In this context, the simulated data from two synthetic models are produced using RESIP2DMODE, an open-source MATLAB code specifically crafted for 2.5D forward modelling of the resistivity and IP data [18]. The apparent electrical resistivity and IP responses of the synthetic models are simulated using a linear dipole-dipole setup, with measurements taken from position 0 up to 420 m and a fixed electrode spacing of 10 m at up to 8 levels (n=1-8, where n indicates the number of receiver-transmitter dipole separations). This results in a total of 132 measurements. For the 2.5-D forward modelling, we partition the model into a series of rectangular cells, where the width of the working-area cells matches the unit electrode spacing, and the depth of the cells logarithmically increases in the vertical direction. To better emulate real-world field conditions, we introduce perturbations into the forward modelling responses, encompassing both apparent resistivity and apparent chargeability data. These perturbations involve the addition of 2% uncorrelated Gaussian-distributed noise with a zero mean, and the magnitude of the noise varies depending on each data point.

Model 1

The initial model, denoted as Example 1, comprises three structures, resembling the inclined vein structures, situated at varying depths beneath the surface. These bodies are embedded within a homogeneous medium characterized by a resistivity of 1000 Ω.m and a chargeability of 1 mV/V, as illustrated in Figure 1. Table 1 provides details regarding the geo-electrical parameters relevant to Example 1. Throughout the inversion process, lower and upper bounding constraints for resistivity values are established as $[\rho^{low} = 0, \rho^{upper} = 5000]$ Ωm for all synthetic examples. Figures 2(a) and 3(a) displays the apparent resistivity and chargeability pseudo-sections, which have been affected by noise. The pseudo-sections do not allow for the accurate identification of the true subsurface structures in terms of geometry and physical properties. Following the strategy proposed for the inversion of apparent resistivity and chargeability data sets, Figures 2(c) and 3(c) show the inverted sections of resistivity and chargeability. In these figures, it is evident that the primary features and structures of the synthetic model are accurately replicated, and no significant undesirable features (artifacts) are observed in the inverted resistivity and chargeability tomograms. Additionally, the top and bottom surfaces of three structures are clearly resolved in the resistivity section.

Table 1. The synthetic geo-electric parameters corresponding to model 1.

Number	Region	$\rho(\Omega m)$	$\eta(mV/V)$
1	Background	1000	1
2	Structure 2	200	15
3	Structure 3	100	50
4	Structure 4	10	100

However, the lower boundary of the third structure (medium 4) is not accurately recovered. In both resistivity and chargeability inversions, the inversion algorithms converge after 20 and 5 iterations, respectively. The root mean square (RMS) data misfit error values for the resistivity and chargeability inversions are 5.32% and 2.4%, respectively.

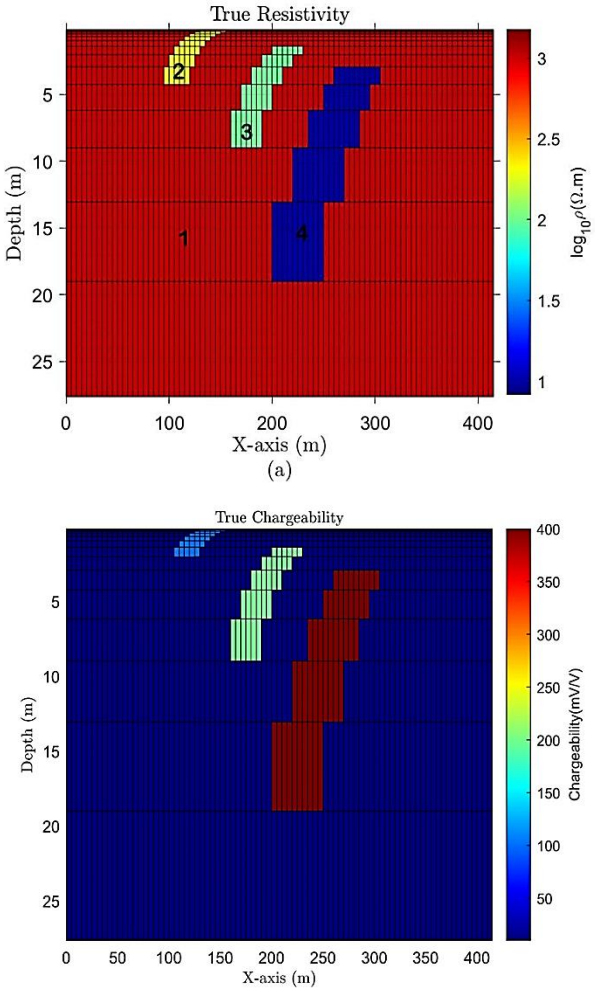

Figure 1. The representation of a) true resistivity and b) true chargeability sections associated with Example 1 containing four different mediums.

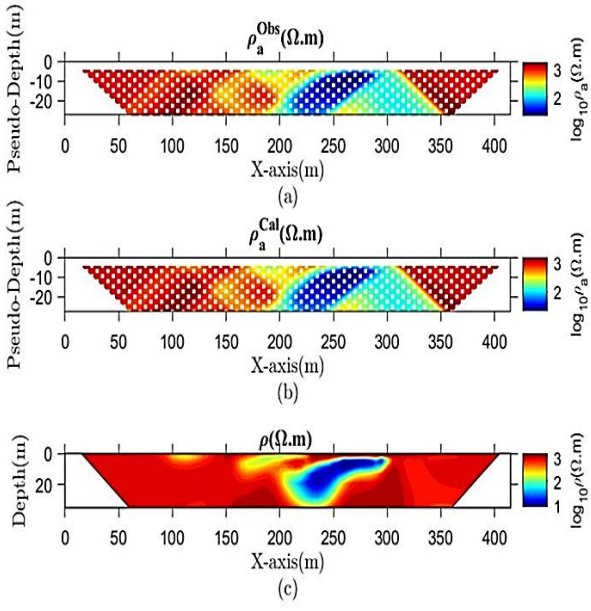

Figure 2. a) The observed apparent resistivity pseudo-section, b) The calculated apparent resistivity pseudo-section, and c) The inverted section of resistivity for the first synthetic model shown in Figure 1(a).

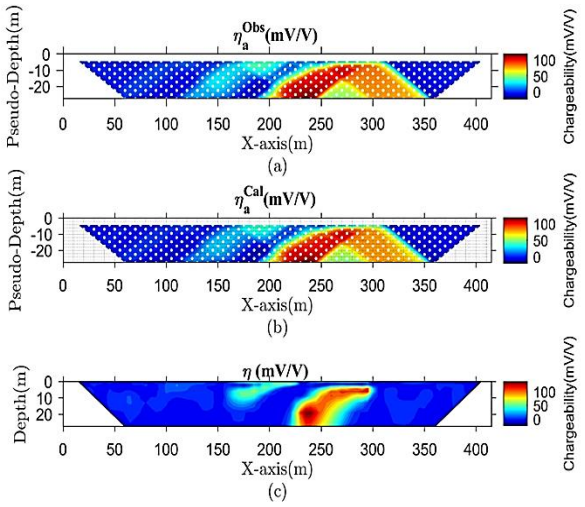

Figure 3. The observed apparent chargeability pseudo-section, b) The calculated apparent chargeability pseudo-section, and c) The inverted section of resistivity for the first synthetic model shown in Figure 1(b).

Model 2

The second synthetic example, denoted as Example 2, is more intricate as it involves four distinct mediums, as shown in Figure 4. A vertical contact in the middle of the model delineates two regions with varying resistivity and chargeability values. Table 2 represents different regions of Example 2 in terms of the resistivity and chargeability. Figures 5(a) and 6(a) illustrate the pseudosections of the apparent resistivity and chargeability corresponding to Example 2. The pseudosections show the expected presence of two distinct regions characterized by differences in the resistivity and chargeability in the central portion of the tomograms. However, the boundary of the vertical contact and the resistive surface layer are not clearly resolved. The observed data are subjected to inversion while adhering to spatial smoothness constraints and the predefined lower and upper bounds. The inversion results for the resistivity and chargeability are presented in Figures 5(c) and 6(c), respectively. These figures demonstrate that the inverted tomograms accurately depict the boundaries of the subsurface structures. In both resistivity and chargeability inversions, the inversion algorithms converge after 18 and 4 iterations, respectively. The RMS data misfit error values for the resistivity and chargeability inversions are 2.35% and 2.8%, respectively.

Table2. The synthetic geo-electric parameters corresponding to model 2.

Number	Region	$\rho(\Omega m)$	$\eta(mV/V)$
1	Medium 1	1000	10
2	Overburden layer 2	200	100
3	Layered medium	100	200
4	Intrusive anomaly	10	400

5.2. Field example

In the previous section, we demonstrated the functionality and accuracy of our inversion algorithm using synthetic data sets. Here, we present a field example to showcase the capability and efficiency of the proposed methodology in real-world scenarios. The study area is situated in the Nikuiyeh region in Qazvin province, Northwest Iran. Geoelectrical measurements, including the resistivity and IP tomography methods were conducted for the exploration of epithermal gold deposits. The study area spans approximately 6.2 Km^2 in Takestan city, west of the Qaqazan district, and is located about 1.5 km southeast of Nikuiyeh village. The predominant style of mineralization in the study area consists of vein-like and veinlet-like zones controlled by faults and fractured zones. In fact, fractured zones provide suitable locations for the accumulation of hydrothermal fluids, resulting in the formation of vein-type, massive, or disseminated deposits of various metallic ores, including gold. The primary constituent of mineralization in the studied area is quartz. Other formation minerals found within it include pyrite,

chalcopyrite, galena-sphalerite, free gold, and secondary weathered oxides. The highest concentration of gold and associated elements is confined to the quartz-sulfide veins and veinlets. The abundance of these elements significantly decreases in the surrounding siliceous-argillaceous parts of the veins and veinlets and reaches a minimum as one moves away from the quartz-sulfide veins and veinlets. In field surveys within the study area, the dipole-dipole array was used. In order to cover the area, a total of 20 dipole-dipole profiles with an electrode spacing of 20 m up to 8 levels were deployed over a one-square-kilometer area. The general procedure for the survey involves initially establishing a baseline as a reference line, typically aligned parallel to the outcrop of the mineral or, more generally, parallel to the appearance of anomalies on the ground. Measurements were then taken perpendicular to this line, essentially perpendicular to the trend of the mineralization zone. Figure 7 shows a simplified geology map of the study area.

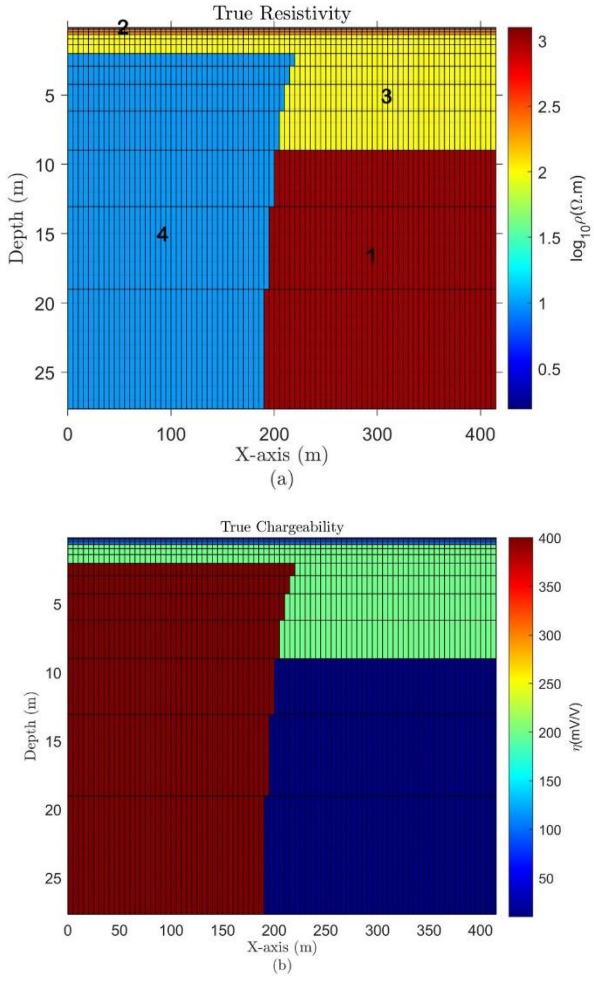

Figure 4. The representation of a) true resistivity and b) true chargeability sections associated with Example 2 containing four different mediums.

When performing field data inversion, we follow the strategy outlined for synthetic examples. Initially, we invert the apparent resistivity data, followed by the non-linear inversion of the IP measurements. Figures 8(a) and 8(b) show a three-dimensional representation of the inversion results of the apparent resistivity and IP data associated with 10 profiles. Note that for representation purposes, only 10 profiles are presented. In areas with a high concentration of metallic or sulfide minerals, the IP response will naturally be the basis for exploration. However, in these areas, electrical resistivity values may not necessarily be low. For example, the presence of copper-bearing minerals in siliceous zones leads to both a high IP response and high electrical resistivity anomalies. The geological alterations in this region are of two types: siliceous and argillic. In the resulting sections obtained through inversion, the presence of sulfide minerals leads to a high IP response, and siliceous alterations increase the resistivity response. Additionally, the presence of clay minerals enhances the membrane-IP response, while argillic alterations result in low electrical resistivity responses. Based on the models obtained from inversion, it is generally observed that silica zones with high resistivity at depths of approximately 10-35 meters tend to exhibit a reduction in resistivity and a relative increase in induced-polarization response. Consequently, it can be stated that with increasing depth of the silica zone, the sulfide mineralization within it has increased. It can be also seen from the resistivity and IP tomograms that the regions with high chargeability areas correspond to those of medium to high electrical resistivity areas.

We also provide a comparison of the resistivity and chargeability tomograms inverted by the commercial software (Geotomo Res2DInv ver. 4.9.18, [19]), for profile 10 of field data, in Figure 9. Visually comparing the resulting tomograms, it is evident that there is a trivial difference between the resistivity and chargeability models obtained from our algorithm and the commercial software.

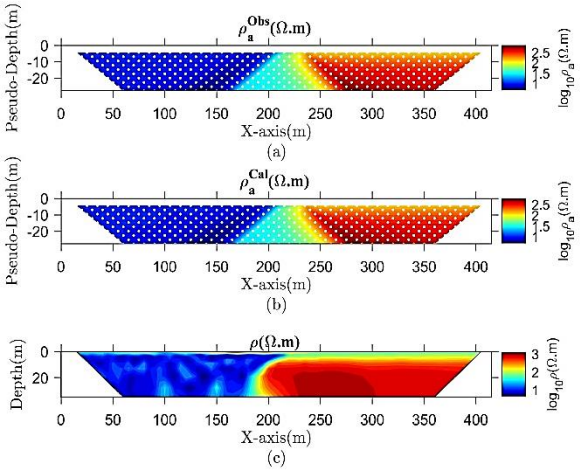

Figure 5. a) The observed apparent resistivity pseudo-section, b) The calculated apparent resistivity pseudo-section, and c) The inverted section of resistivity for the second synthetic model shown in Figure 4(a).

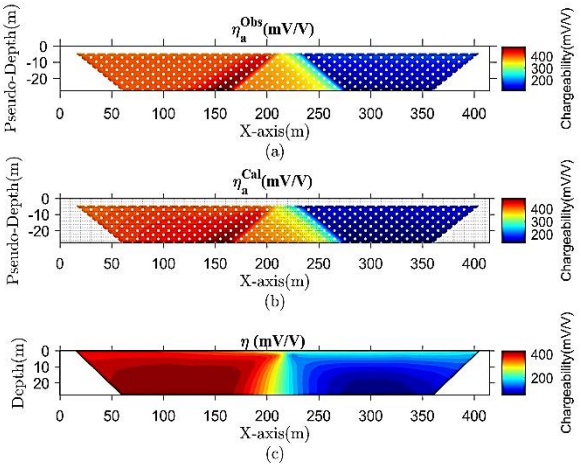

Figure 6. The observed apparent chargeability pseudo-section, b) The calculated apparent chargeability pseudo-section, and c) The inverted section of resistivity for the second synthetic model shown in Figure 4(b).

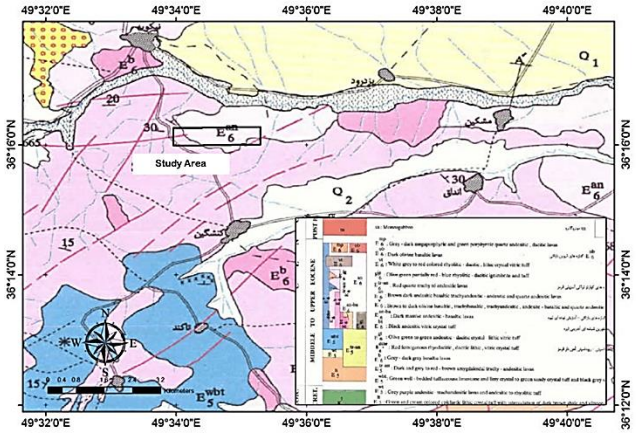

Figure 7. The geology map of the study area, 1:100000. The study area is displayed by a black rectangular.

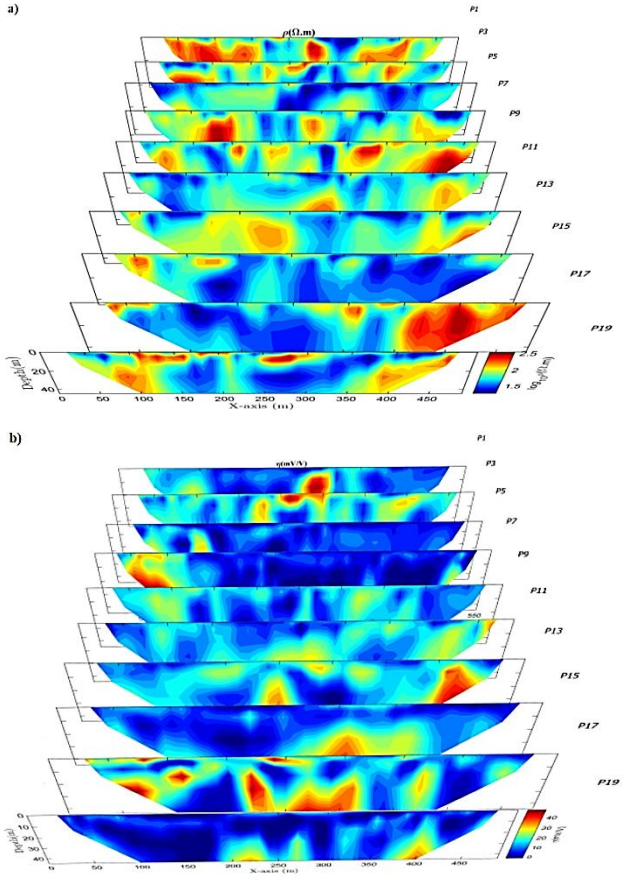

Figure 8. A 3D representation of a) resistivity and b) chargeability sections. Note that for the purpose of representation, only 10 inverted sections are displayed.

6. Conclusion

Given the significance of the inversion process in ensuring a reliable imaging of subsurface features in chargeability models, this paper concentrates on the inversion of time-domain IP data. We introduce a two-step approach for the inversion of IP data. In the first step, the resistivity data undergo inversion, and in the second step, a non-linear chargeability inversion is employed to retrieve the polarizability model. In this non-linear inversion, the inherent non-linearity of the problem is addressed through linearization using a sensitivity matrix consisting of partial derivatives of measurements concerning model parameters.

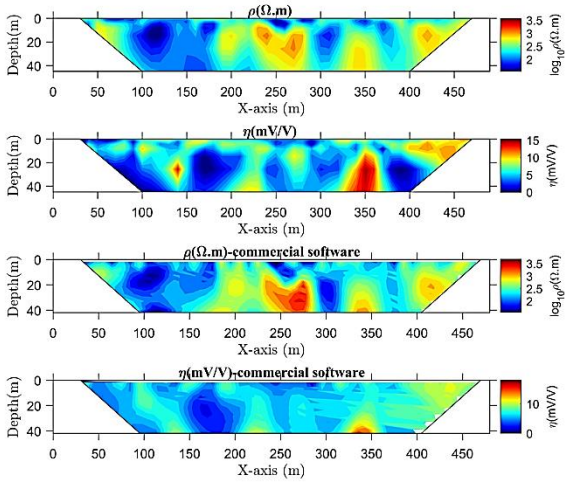

Figure 9. The resistivity and chargeability sections obtained using the proposed algorithm, (a),(b) and the commercial software, (c),(d) (Geotomo Res2DInv ver. 4.9.18), profile 10.

To evaluate the efficiency and precision of our developed IP inversion code package, which encompasses the forward modelling algorithm, sensitivity matrix computation, and inversion algorithm, we conducted tests using synthetic data examples and real field data. The numerical outcomes revealed that the presented inversion algorithm consistently delivers reliable inversion results, faithfully capturing the essential characteristics and structures of the models while avoiding the generation of spurious effects. In essence, beyond the theoretical aspects outlined in this paper, the primary contribution of this study lies in its ability to enhance the resolution of subsurface structures in terms of the resistivity and chargeability distribution via a smoothness-constrained inversion approach, all the while preventing the introduction of extraneous features (artifacts) into the inverted models.

REFERENCES

[1] Sumner, J. S. (1976). Principles of Induced Polarization for Geophysical Exploration. Elsevier: Amsterdam.

[2] Bertin, J., & Loeb, J. (1976). Experimental and Theoretical Aspects of Induced Polarization. Volume I: Presentation and Application of the IP Method, Case Histories. Gebrüder Borntraeger: Berlin.

[3] Fink, J. B., McAlister, E. O., Sternberg, B. K., Wieduwilt, W. G. & Ward, S. H. (1990). Induced polarization: applications and case histories Investigations in Geophysics. Society of Exploration Geophysicists, Tulsa. DOI: 10.1190/1.9781560802594.

[4] Pelton, W. H, Rijo, L, & Swift, J. R, (1978). Inversion of two-dimensional resistivity and induced polarization data. Geophysics, 43(4), 681-904.

[5] Sasaki, Y. (1982). Automatic interpretation of induced polarization data over two-dimensional structures. Memories of the Faculty of Engineering, Kyudshu University, 42, 59–74.

[7] Seigel, H. O. (1959). Mathematical formulation and type curves for induced polarization. Geophysics, 24, 547-565.

[8] Oldenburg, D. W. & Li, Y. (1994). Inversion of induced polarization data, Geophysics, 59

(9), 1327–1341.

[9] La Brecque, D. J. (1991). IP tomography. 61st Annual International Meeting SEG, Expanded Abstracts, 413-416.

[10] Hohmann, G. W. (1990). Three dimensional IP models.

Investigations in Geophysics, Society of Exploration Geophysicists.

[11] Beard, L. P., Hohmann, G. W., & Tripp, A. C. (1996). Fast resistivity/IP inversion using a

low-contrast approximation. Geophysics, 61(1), pp. 169–179

[12] Li, Y., & Oldenburg, D. W. (2000). 3-D inversion of induced polarization data. Geophysics, 65(6), 1931–1945.

[13] Karaoulis, M., Revil, A., Tsourlos, P., Werkema, D. D., & Minsley, B. J. (2013). IP4DI: A software for time-lapse 2D/3D DC-resistivity and induced polarization tomography. Computers & Geosciences, 54, 164-170.

[14] Ghanati, R., & Fallahsafari, M. (2022). Fréchet derivatives calculation for electrical resistivity imaging using forward matrix method. Iranian Journal of Geophysics, 15(4), 153-163.

[15] Dey, A., & Morrison, H. F. (1979). Resistivity modeling for arbitrary shaped two-dimensional structures, Geophysical Prospecting, 27, 1020–1036.

[16] Fallahsafari, M., & Ghanati, R. (2022). DC Electrical Resistance Tomography Inversion. Journal of the Earth and Space Physics, 47(4).

[17] Dahlin, T. & Loke, M. H. L. (2015). Negative apparent chargeability in time-domain induced polarisation data. Journal of Applied Geophysics, 123, 322-332.

[18] Ghanati, R., Azadi, Y., & Fakhimi, R. (2020). RESIP2DMODE: A MATLAB-Based 2D Resistivity and Induced Polarization Forward Modeling Software. Iranian Journal of Geophysics, 13(4), 60-78.

[19] Loke, M. (2019). Geotomo software, [Online]. Available: http://geotomosoft.com/.